A Comprehensive Study on the Parameters Affecting Magnesium Plating/Stripping Kinetics in Rechargeable Mg Batteries

Muath Radi, Taniya Purkait, Deyana S Tchitchekova, Alejandro R Goñi, Robert Markowski, Charlotte Bodin, Cecile Courreges, Rémi Dedryvère, Alexandre Ponrouch

ADVANCED ENERGY MATERIALS
www.advenergymat.de

A Comprehensive Study on the Parameters Affecting Magnesium Plating/Stripping Kinetics in Rechargeable Mg Batteries

Muath Radi, Taniya Purkait, Deyana S. Tchitchekova, Alejandro R. Goñi, Robert Markowski, Charlotte Bodin, Cécile Courrèges, Rémi Dedryvère, and Alexandre Ponrouch**

Mg metal anode-based battery is a more sustainable, lower cost, and higher energy density alternative to Li-ion. However, this battery chemistry also faces several challenges associated with the high charge density of Mg^{2+}, including achieving high reversibility and low voltage hysteresis for Mg metal plating/stripping. While significant improvements are achieved in last decades, they involve rather complex electrolyte formulations and/or Mg salts difficult to produce, and the use of unpractical substrates such as platinum. Here, significant improvement in terms of Mg plating kinetics is achieved in electrolytes containing commercial magnesium bis(trifluoromethanesulfonyl)imide salt ($Mg(TFSI)_2$) by using titanium substrate with similar crystal structure and lattice parameter as Mg leading to lower nucleation overpotential. Low salt concentration electrolyte and addition of dibutyl magnesium ($Mg(butyl)_2$) also enable the formation of thinner interphase, richer in solvent based decomposition products, further improving Mg plating kinetics. This work highlights the complex role of $Mg(butyl)_2$, often considered as a simple drying agent, and how it impacts ion solvation favoring the mobility of electroactive cationic species, paving the way toward better electrolyte design with improved cation transference number.

1. Introduction

A general agreement today is that mainstream electrical storage technologies are unlikely to be sufficient to meet the requirements for decentralization and decarbonization networks, and a restricted focus on Li-ion batteries is putting the development of more cost-effective alternative technologies at risk.[1] Among intensively investigated alternatives, the Mg metal anode based technology has great prospect considering the low reduction potential of Mg metal, −2.372 V versus standard hydrogen electrode (SHE), its high volumetric capacity of 3833 mAh cm^{-3}, nearly twice that of the Li-metal analog (2062 mAh cm^{-3}), and its relative abundance in the earth's crust of ca. 2.3% (roughly three orders of magnitudes higher than Li with ca. 0.002%).[2,3] Thus, the starting materials are much more available and cheaper. Despite these promising characteristics, improving the current Mg anode performances is strenuous, mainly due to the ionically passivating interphase formed upon exposure of the Mg surface to electrolytes, preventing further Mg deposition. The first rechargeable Mg prototype battery was reported in 2000 using Grignard reagents as electrolytes demonstrated as stable versus the Mg metal electrode,[4] the downside of these halides based complex

M. Radi, C. Courrèges, R. Dedryvère
IPREM
E2S-UPPA
CNRS
Université de Pau & Pays de l'Adour
2 AV du Président Pierre Angot, Pau 64053, France
E-mail: remi.dedryvere@univ-pau.fr

The ORCID identification number(s) for the author(s) of this article can be found under https://doi.org/10.1002/aenm.202401587

DOI: 10.1002/aenm.202401587

T. Purkait, D. S. Tchitchekova, A. R. Goñi, R. Markowski, C. Bodin, A. Ponrouch
Institut de Ciència de Materials de Barcelona
ICMAB-CSIC
Campus UAB, Bellaterra 08193, Spain
E-mail: aponrouch@icmab.es

A. R. Goñi
ICREA
Passeig Lluís Companys 23, Barcelona 08010, Spain

C. Bodin, R. Dedryvère, A. Ponrouch
ALISTORE – European Research Institute – CNRS FR 3104
Amiens Cedex 80039, France

R. Dedryvère
RS2E
Réseau Français sur le Stockage Electrochimique de l'Energie
FR CNRS 3459
Amiens Cedex 80039, France

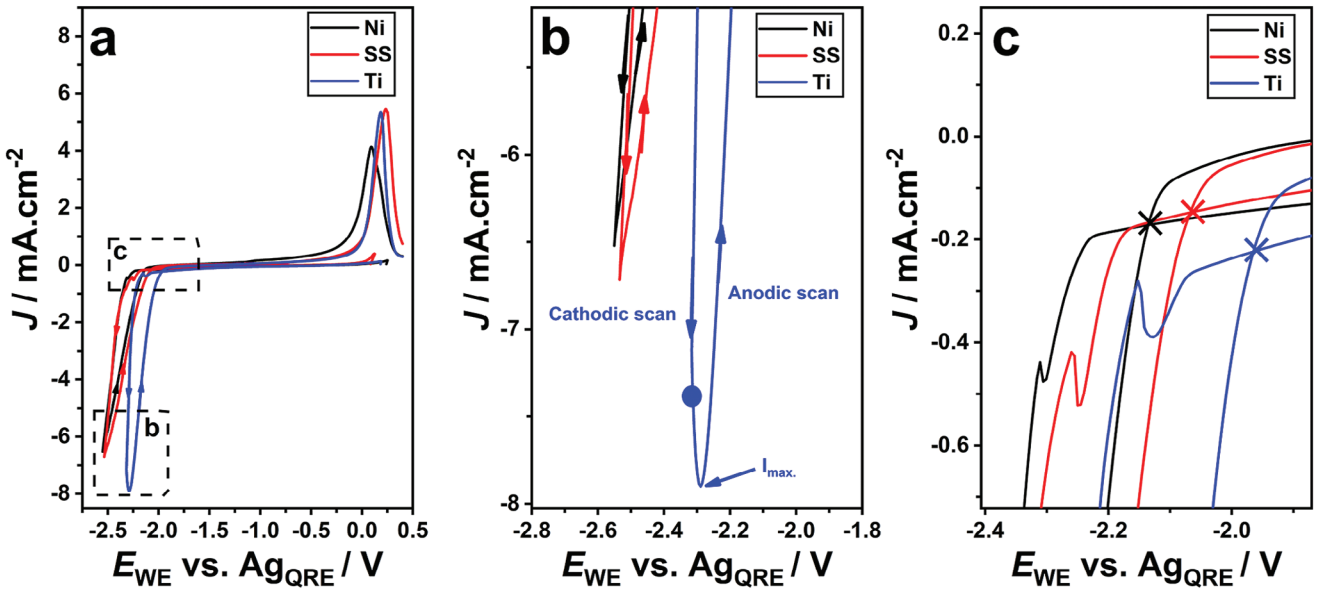

Figure 1. a) Cyclic voltammograms at 10th cycle of three different electrodes (Ni, stainless steel (SS) and Ti) using 0.4 M $Mg(TFSI)_2$ in G1:G2 electrolyte with a scan rate of 25 mV s^{-1}. b,c) are magnified spectra of the two selected regions in inset (a), showing the current maximum reached during the anodic scan (the blue circle represents the end of the cathodic scan) and the cross-over potentials (indicated by cross signs ×), respectively.

electrolytes being their very low potential window for practical use, and their corrosiveness. As a result, the MACC (magnesium aluminum chloride complex), an all inorganic electrolyte was developed,[5–7] yet it is impractical owing to its complicated and expensive synthesis procedure, sensitivity to air and moisture, and low ionic conductivity.

An appealing alternative is to use Mg salts containing weakly coordinating anions like $TFSI^-$, which is commercially available, halide free, have better solubility in aprotic ethereal solutions and high ionic conductivity (5.22×10^{-3} S cm^{-3} for 0.5 M $Mg(TFSI)_2$ in monoglyme/diglyme, G1/G2) as well as wide electrochemical window.[8,9] However, decomposition of $Mg(TFSI)_2$ based electrolytes (i.e., salt and solvent) and the reaction of trace moisture with Mg electrode passivate the Mg surface, resulting in prohibitive overpotential of Mg plating/stripping and low Coulombic efficiency.[9–11] DFT calculations demonstrated that the $Mg(G1)_3^{2+}$ solvates formed in the $Mg(TFSI)_2$/G1 electrolyte partially decompose at the anode surface, forming inactive $Mg(OCH_3)_2(G1)_2$ products and ethylene.[12] Another pathway for electrolyte degradation and Mg electrode passivation arises from the anion decomposition favored by the presence of $MgTFSI^+$ contact ion pairs (CIP),[13] the latter being facilitated by the high charge density of the divalent cations and by higher salt concentration in solution.[14]

Here, we demonstrate that several factors, such as the substrate crystallographic structure, the cycling history, the electrolyte concentration and the presence of additive (dibutyl magnesium, $Mg(butyl)_2$), can impact the Mg plating/stripping voltage hysteresis and coulombic efficiency. Furthermore, the correlation between the composition of Mg electrode passivation layer and the cell electrochemical performance is revealed.

2. Results and Discussion

2.1. The Influence of the Substrate Nature

Precious metals like Au or Pt are commonly used as substrates because of their presumably inert surface even though they are irrelevant for practical rechargeable Mg battery applications. Here we explore the kinetics of Mg plating/stripping on three non-precious metal substrates, namely Ti, Ni and SUS316L stainless steel (SS), using 0.4M $Mg(TFSI)_2$ dissolved in G1:G2 (1:1 vol) mixture, and the corresponding cyclic voltammograms (CVs) are shown in **Figure 1a** (the 10th cycle is used for comparison, the first cycle being shown in Figure S1, Supporting Information). Upon cathodic scan (toward negative potential values), all CVs present a strong reduction current below −2.0 V versus Ag quasi reference electrode (Ag_{QRE}). Upon anodic scan (toward high potential values), a reduction current maximum is observed (I_{max}), which is most discernible in the case of Mg deposition on Ti, as shown in Figure 1b (the blue circle in the figure represents the end of the cathodic scan). A cross-over potential is recorded with all three substrates, i.e., the plating current during the anodic scan is higher as compared to the cathodic scan (Figure 1c). This behavior is usually observed when the cathodic scan is stopped before coalescence of the growing crystals.[15] This shape is thus linked to the plating mechanism. Finally, above −0.4 V versus Ag_{QRE} an oxidation peak corresponding to Mg stripping is observed. All three studied substrates show typical features of metallic electrodeposition, the steepest plating/stripping current profile being achieved with Ti. However, in all cases, a prohibitive voltage hysteresis of >1.5 V is measured between Mg plating and stripping, which is common for $Mg(TFSI)_2$ based electrolytes.[16] Ti was purposely introduced here due to its structural similarity to metallic Mg. Indeed, by contrast to most conventional

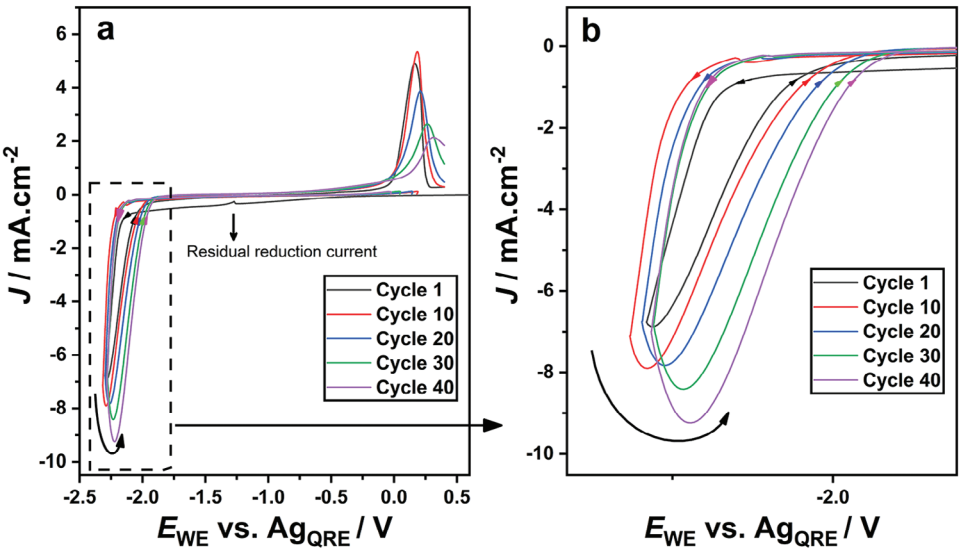

Figure 2. a) Cyclic voltammograms of a Ti electrode using 0.4 M $Mg(TFSI)_2$ in G1:G2 electrolyte with a scan rate of 25 mV s^{-1} at several cycle numbers. b) Magnification of selected region in inset (a), showing the increase in the plating current during the anodic scan with further cycling.

substrates (Cu, Al, Ni, SS, Pt, Au, etc.) which have cubic structures, Mg and Ti crystallize in hexagonal close-packed structures with similar lattice parameters (a = b = 3.2 Å and c = 5.2 Å for Mg and a = b = 2.95Å and c = 4.68Å for Ti). The effect of lattice matching is twofold: it can improve the deposit adhesion (by reducing interfacial mechanical stress) and reduce the nucleation overpotential,[17] hence Ti was selected as the substrate for further investigations. It is worth mentioning that Ti is a rather expensive metal (6.6 USD/kg in 2024), which would be detrimental for application as current collector in batteries. However, Cu which is commonly used in commercial Li-ion cells is not significantly cheaper (4.2 USD/kg in 2024) and is considerably less abundant on the earth crust (25th most abundant element vs 9th for Ti) leading to much higher price volatility. In addition, the lower density of Ti (4.5 g cm^{-3}) compared to Cu (8.93 g cm^{-3}) implies that, for similar foil thickness, lighter and possibly less expensive Ti current collector could be used in Mg batteries compared to Cu in Li-ion.

During the first cycle, a residual reduction current was recorded before plating starts (**Figure 2a**), which may indicate contribution from capacitive current (adsorption of ions on the electrode) or partial electrolyte decomposition. This residual reduction current disappears after the first cycle, suggesting the formation of a passivation layer preventing further electrolyte decomposition or capacitive processes. Upon cycling, the stripping peak broadens and continuously shifts toward higher potential values, eventually resulting in loss of charge associated with Mg stripping and accumulation of metallic Mg at the surface of the substrate. By contrast, the onset potential for plating and the plating kinetics (i.e., the slope of the reduction wave) remain unchanged during cycling. The increase in the overall plating current upon cycling observed in Figure 2b is tentatively attributed to the continuous accumulation of non-stripped Mg resulting in increased surface area.

In order to investigate the possible electrolyte degradation and formation of passivation layer, X-ray Photoelectron Spectroscopy (XPS) measurements were performed on Ti electrodes stopped after 5 and 50 cycles at the end of reduction (**Figure 3**).

Firstly, from the Ti 2p spectrum, the Ti substrate still can be detected at the end of the 5th reduction scan, which means the substrate has not been totally covered by Mg deposit. The shape of this Ti 2p spectrum is in good agreement with the spectrum recorded for the fresh substrate (see Figure S3, Supporting Information). After 50 cycles, the Ti substrate is no more detectable, consistent with Mg accumulation at its surface, as concluded from CV curves and confirmed by the detection of the Mg^0 signal in Mg KLL Auger spectrum, but also with the growth of a covering layer at the Ti surface from electrolyte decomposition products. Indeed, the small amount of metallic Mg detected in the electrode by XPS can be rationalized by the presence of a relatively thick layer, passivating its surface. Such decomposition film can be formed either concomitantly with the Mg plating and/or after its deposition due to the reactivity of the metallic Mg with the electrolyte.

The degradation of the salt is evidenced by the presence of several reduced sulfur species in the S 2p spectra. A greater proportion of these reduced species after 50 cycles indicates further reduction (degradation) of the electrolyte upon prolonged cycling. Especially, MgS is detected after 50 cycles. Moreover, F 1s spectra show higher amounts of MgF_2 (9%) after 50 cycles with respect to 5 cycles (4.5%), as deduced from Table S1 (Supporting Information).

The C 1s spectra show that the surfaces of both electrodes are covered by the same chemical species: hydrocarbon (~285 eV), organic constituents containing C–O and COO environments, a carbonate environment probably due to $MgCO_3$, and CF_3 groups from the salt. Regardless of this qualitative similarity, the surface of the electrode stopped after 50 cycles was covered with more carbonate (12%) than the one at 5 cycles (7%) (see Table S1, Supporting Information). The O 1s spectra show all the local environments of oxygen present at the surface of the substrates, with oxygen atoms bound to carbon (C-O and COO environments), as

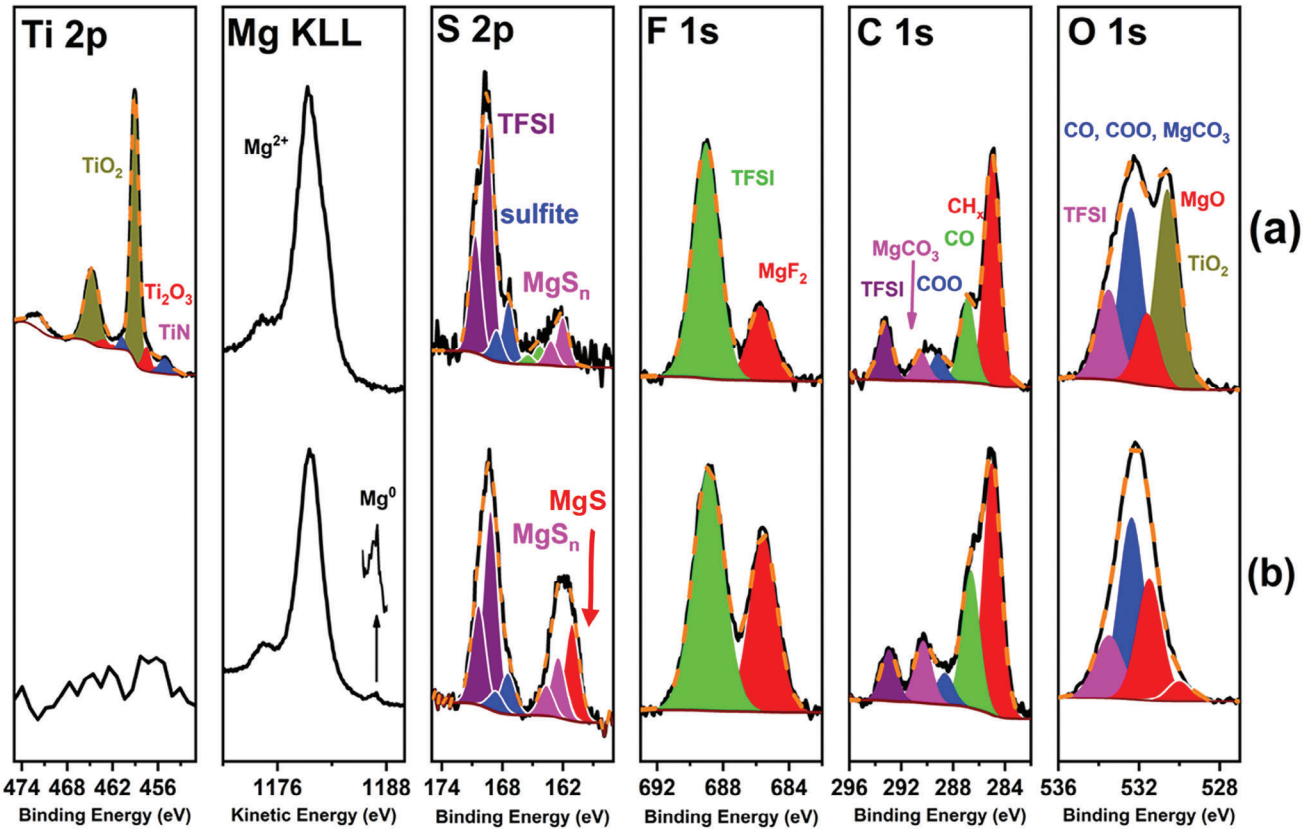

Figure 3. XPS Ti 2p, S 2p, F 1s, C 1s, O 1s, and Auger Mg KLL spectra of Mg deposits formed on Ti electrodes cycled in 0.4 M $Mg(TFSI)_2$ electrolyte: a) at the end of 5th plating scan, b) at the end of 50th plating scan. The solid and dashed lines represent the measured and fitted data, respectively.

well as oxygen from the salt. Additionally, the electrode stopped after 5 cycles shows the oxygen from the substrate (TiO_2). For both electrodes, an extra O 1s (red) component at ≈531.5 eV is attributed to MgO. This component is necessary for the correct fit of the spectra, and cannot be attributed to $Mg(OH)_2$ due to the observed quantitative O to Mg ratio, which is equal to one. Actually, this MgO component appears at a higher binding energy (B.E.) than expected (≈530 eV). This can be explained by the direct electronic contact of this very thin MgO layer with the Mg metallic surface, as also observed for different oxides, resulting in a shift in the binding energy[18–27] (see the supporting information for more explanation and justification of our attributions). For the electrode stopped after 50 cycles, an additional weak peak at lower B.E. (≈530 eV) is also attributed to MgO, the existence of two peaks for the same compound being explained by the increase in the MgO thickness: indeed, if the thickness is great enough, the outermost part of MgO is no more in electronic contact with the metal underneath and is no more shifted.

Thus, the presence of a passivation layer is confirmed through both electrochemistry (capacitive current) and XPS, and it grows with further cycling, as indicated by the accumulation of reduction species at the electrode surfaces (sulfur species, MgF_2, $MgCO_3$, MgO etc.). This continuous growth of the passivation layer explains the drop of the stripping current with cycling.

2.2. The Influence of the Electrolyte Concentration

It was previously reported that "free" $TFSI^-$ anion in solution is stable against the Mg metal electrode, while its reductive decomposition is favored when coordinated in $MgTFSI^+$ CIP.[13,28,29] The presence of anion decomposition products evidenced by our XPS data therefore points at some degree of ion pairing in this electrolyte. Accordingly, we further explored the possibility to engineer the Mg^{2+} solvation shell through modification of the salt concentration. **Figure** 4a illustrates the CV of Ti electrodes in glyme-based electrolyte with $Mg(TFSI)_2$ salt concentrations ranging from 0.1 up to 0.4 M. Interestingly, the 0.1 M concentration shows a distinct plating/stripping profile with lower overpotential compared to the higher electrolyte concentrations, but the kinetics of plating and stripping remain sluggish with evidence for mass transport limitation (a peak appears during the cathodic scan), possibly because of unavailability of Mg^{2+} at the electrode surface.

With prolonged cycling, however, the overall kinetics at 0.1 M is significantly improved as evidenced in Figure 4b, with a steeper reduction wave slope and cross-over potentials being observed again. Although Mg stripping appears as a very broad peak, spreading over 1 V, much lower voltage hysteresis (350 mV) between the onset potentials for plating (ca. −1.6 V vs Ag_{QRE}) and for stripping (ca. −1.25 V vs Ag_{QRE}) was recorded, which is remarkably low for a $Mg(TFSI)_2$ based electrolyte without

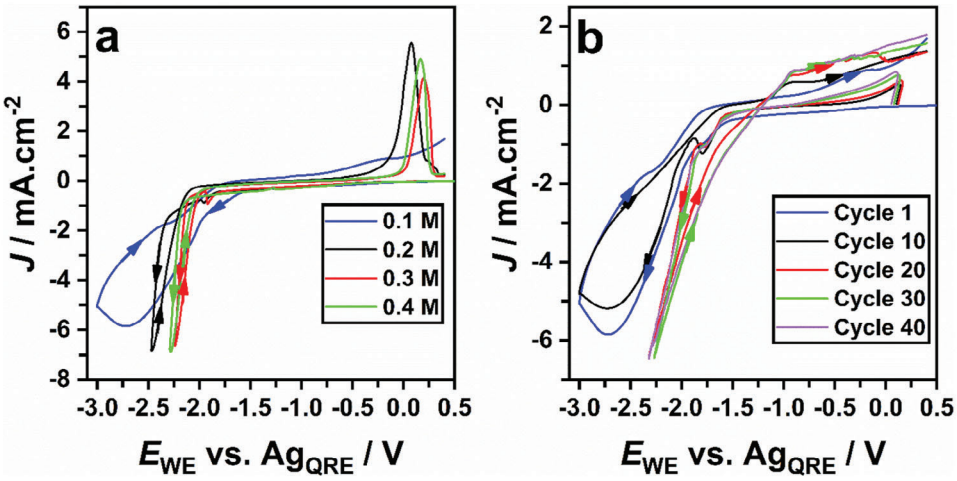

Figure 4. a) Cyclic voltammograms (first cycle) of Ti electrodes using different concentrations of $Mg(TFSI)_2$ salt in G1:G2 mixture with a scan rate of 25 mV s^{-1}. b) Cyclic voltammograms of a Ti electrode using 0.1 M $Mg(TFSI)_2$ electrolyte with a scan rate of 25 mV s^{-1} at several cycle numbers.

halogenated additives.[16] In order to better understand this behavior observed for the 0.1 M concentration, we proceeded with XPS analysis of the surface of the deposit obtained at this concentration.

Figure 5a,b displays XPS Ti 2p, F 1s, C 1s, O 1s and Auger Mg KLL spectra of Ti electrodes at the end of 50th plating scan (cathodic scan) using 0.4 and 0.1 M concentrations of $Mg(TFSI)_2$ salt, respectively, while the corresponding Mg 2p, S 2p and N 1s spectra are shown in Figure S5 (Supporting Information). A difference between the two electrodes is that a small metallic Mg signal can be detected in the Mg KLL spectrum for 0.4 M, but not in the case of 0.1 M concentration. This can be ascribed to the sluggish plating kinetics at 0.1 M as discussed for Figure 4. By comparing the C 1s, O 1s, and F 1s spectra, there is no qualitative difference in the surface chemical composition of the two deposits. For instance, both of them include organic constituents containing C–O and COO environments, $MgCO_3$, several reduced sulfur species, MgO, and MgF_2. However, the surface of the deposit in 0.1 M contains less inorganic species than the 0.4 M: 9 versus 12 at.% of $MgCO_3$, 20 versus 25 at.% of MgO, and 8 versus 9 at.% of MgF_2, as deduced from Table S1 (Supporting Information). Therefore, the passivation layer formed in 0.1 M solution appears to be richer in solvent based decomposition products, while the passivation layer formed in 0.4 M electrolyte is richer in anion decomposition products. This could be rationalized by the tendency to form contact ion pairs when salt concentration is increased,[14,16] the coordinated anions being more easily reduced at the substrate surface, leading to the breaking of the C–S bond between O = S = O and CF_3 groups.[13,29,30] Unfortunately, presence of $MgTFSI^+$ CIP could not be confirmed or infirmed by Raman measurements at these two $Mg(TFSI)_2$ concentrations in the G1:G2 mixture (see Figure S10, Supporting Information and related discussion in Section 2.4). Besides, at higher electrolyte concentrations, more impurities are expected, especially more water traces, thus promoting the salt degradation.[11] Indeed, OH^- ions forming at the MgO surface from water traces, can weaken the C-S bond in the $[Mg^{2+}—TFSI^-]^+$ complex via a nucleophilic attack[31–33] and aggravate the passivation process of the Mg surface, leading to a dramatic increase in the stripping overpotential and a decrease in the overall deposition/stripping process efficiency. Additionally, H_2O influences the kinetics of Mg deposition, as it is capable to alter the solvation structure of Mg^{2+} ions in the double layer, forming strongly bound H_2O-Mg^{2+}complexes,[11] which require an extra plating overpotential to initiate Mg deposition, further favoring the $TFSI^-$ degradation.

Going back to Figure 5a,b, it is worth mentioning that the substrate surface in both cases is not detectable anymore, indicating it is fully covered by a passivation layer of greater thickness than the XPS probing depth (≈5-10 nm). This means that the presence of this passivation layer does not hinder the plating/stripping reversibility improvement observed in Figure 4b when decreasing the salt concentration. Moreover, the surface composition of the electrode at the end of the 50th stripping scan (Figure 5c) is very similar to that observed at the end of the 50th plating scan (Figure 5b). In both states, the surface consists of the same chemical components with similar quantities, as shown in Table S1 (Supporting Information), indicating that the passivation layer is stable upon cycling.

2.3. The Influence of Dibutyl Magnesium Addition

Although all prepared electrolytes were carefully dried before cell assembly (see experimental section) and contained less than 5 ppm of water (as per Karl Fisher titration measurements), the use of a conventional drying agent such as dibutyl magnesium ($Mg(butyl)_2$) was explored. $Mg(butyl)_2$ being a strong reducing agent serves as a scavenger to eliminate traces of water,[9,35] but also potential organic impurities originating from glymes.[36]

Cyclic voltammograms of Ti electrodes in 0.1 M $Mg(TFSI)_2$ in G1:G2 electrolytes containing 130 mM of $Mg(butyl)_2$ are presented in **Figure 6**a. The main difference observed after addition of $Mg(butyl)_2$ is the quasi absence of overpotential between plating and stripping (below 50 mV), already at the first cycle, without any conditioning procedure prior to CV. The overpotential gradually increases upon cycling with ca. 100 and 120 mV for cycles

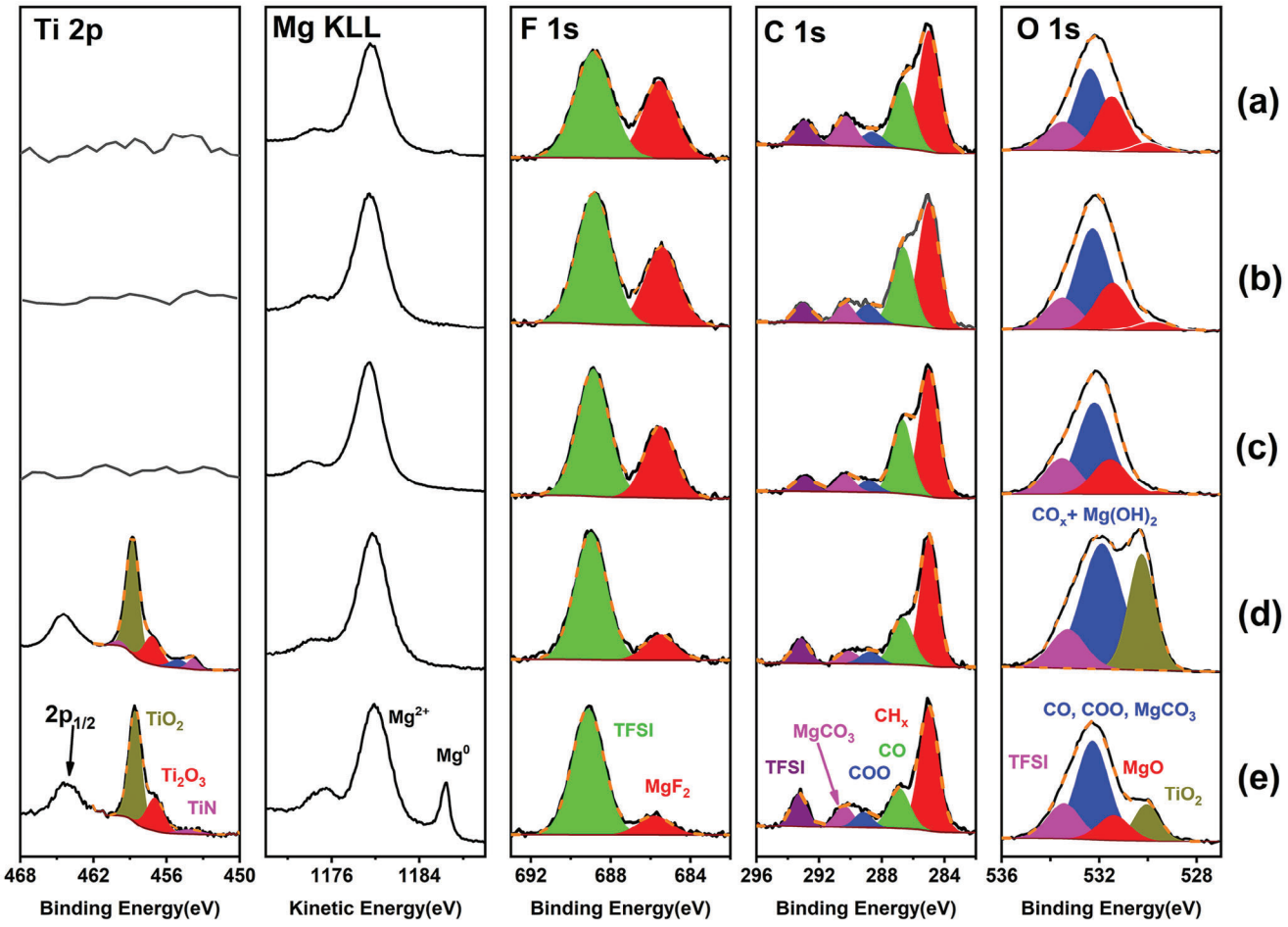

Figure 5. XPS Ti 2p, F 1s, C 1s, O 1s, and Auger Mg KLL spectra of the Mg deposits formed on Ti electrodes in the following conditions: a) 0.4 M $Mg(TFSI)_2$ at the end of 50th plating scan; b,c) 0.1 M $Mg(TFSI)_2$ at the end of 50th plating and stripping scans, respectively; d) 0.1 M $Mg(TFSI)_2$ + 130 mM of $Mg(butyl)_2$ at the end of 50th stripping scan; e) 0.1 M $Mg(TFSI)_2$ + 130 mM of $Mg(butyl)_2$ after 250th stripping scan followed by 10 min of Mg potentiostatic deposition at −1.0 V versus Ag_{QRE}.

5 and 10, respectively. However, it appears to reach a stable value of ≈180 mV after the 20th cycle. To the best of our knowledge, this overpotential value is the lowest ever reported for a $Mg(TFSI)_2$ based electrolyte, pointing at the combination of low salt concentration and the use of $Mg(butyl)_2$ as very promising for Mg metal anode based batteries. While the coulombic efficiency for this non optimized system still requires improvements (for instance via glymes distillation[36]) and reaches 87% after 20 cycles (Figure 6a), a symmetric Mg/Mg cell can cycle (Figure 6b–e) for extended period of time even though very limited amount of electrolyte was used (<140 µL).

Figure 5d illustrates the XPS spectra obtained at the end of the 50th stripping scan when adding 130 mM of $Mg(butyl)_2$. The quantification data are shown in Table S2 (Supporting Information). It can be noticed from Ti 2p spectrum that the Ti substrate is detectable, which means either that the interphase is very thin or it is not totally covering the electrode surface. From Mg KLL, the metallic Mg is not detectable which is not surprising because it is expected that all deposited Mg has been stripped at this stage. However, the addition of $Mg(butyl)_2$ changes the composition of the surface, and the C 1s spectrum shows that the amount of carbonate is divided by two compared to the interphase formed without $Mg(butyl)_2$. While degradation of the salt is still detected from F 1s (Figure 5c,d) and S 2p spectra (Figure S5c,d, Supporting Information), the amounts of MgF_2 (2.5 at.% vs 7 at.%) and of reduced sulfur species (0.3 at.% vs 2.3 at.%) are significantly lower for the sample cycled with $Mg(butyl)_2$. The O 1s spectrum shows oxygen from the Ti substrate (TiO_2, Ti_2O_3) and from carbonaceous groups (C-O, COO), as well as oxygen from the salt. Interestingly, based on the observed quantitative ratio between O and Mg, this electrode surface does not contain MgO, but a great amount of $Mg(OH)_2$ (~24 at.%) at the same binding energy as CO_x groups, i.e., corresponding to the unresolved blue peak at ≈532 eV (Figure 5d). In summary, XPS data indicate that usage of $Mg(butyl)_2$ in the electrolyte formulation produces a thinner passivation layer with less inorganic components and containing $Mg(OH)_2$ instead of MgO.

Complementary Time-of-Flight Secondary Ion Mass Spectrometry (ToF-SIMS) analysis was conducted on the surface of Mg deposits derived from a 0.1 M $Mg(TFSI)_2$ electrolyte, both with and without the addition of 130 mM $Mg(butyl)_2$, as illustrated in Figure S6 (Supporting Information). ToF-SIMS

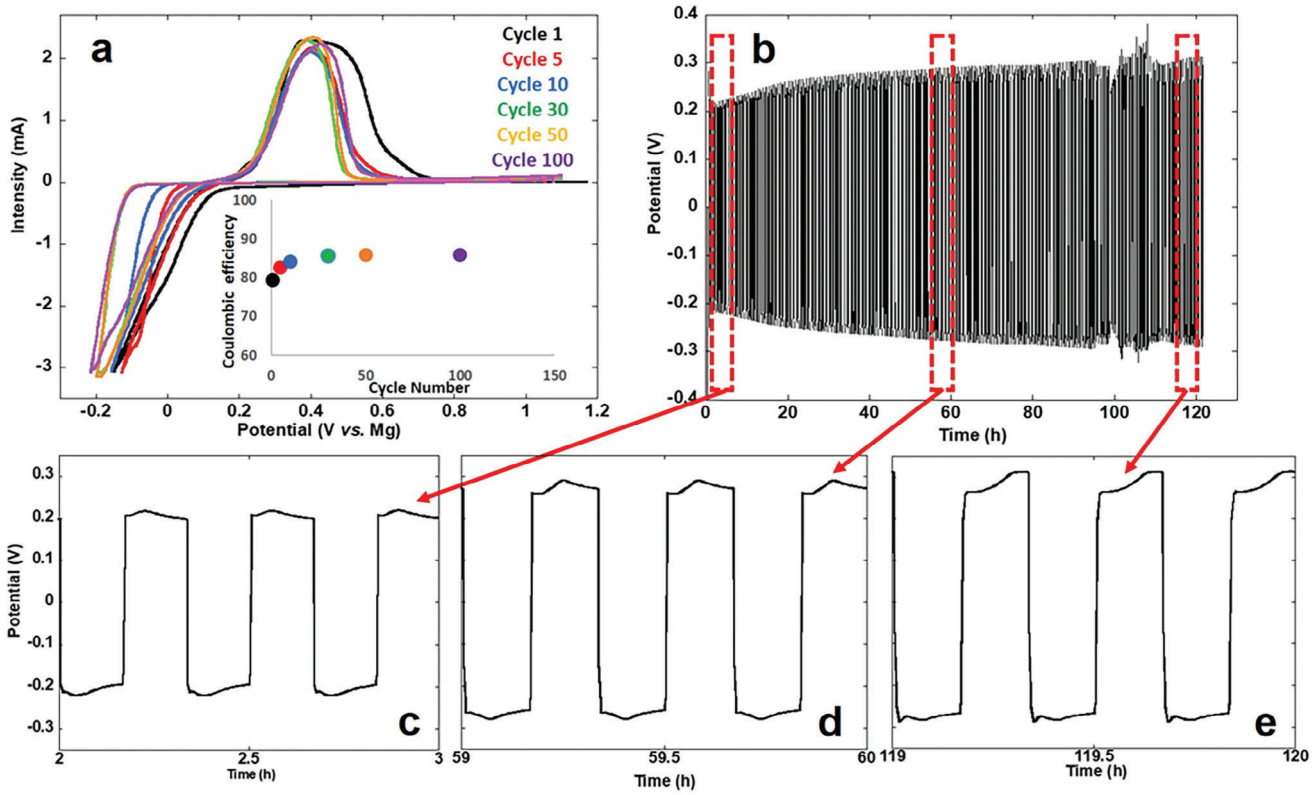

Figure 6. a) Cyclic voltammograms (cycles 1 to 100) of a Ti electrode in 0.1 M $Mg(TFSI)_2$ electrolyte with 130 mM of $Mg(butyl)_2$ (25 mV s^{-1}). b–e) Charge/discharge curves of symmetric Mg/Mg cell cycled in similar electrolyte at 0.1 mA cm^{-2}.

measurements (Figures S6–S9, Supporting Information and full description in Supporting Information) point at the addition of $Mg(butyl)_2$ to the electrolyte decreasing both inorganic and organic components of the passivation layer on the Mg deposits consistent with the general conclusions from XPS. It is worth mentioning that similar trends toward thinner passivation layer in $Mg(TFSI)_2$ based electrolytes was also achieved in amine co-solvent containing electrolytes.[37]

For the electrode obtained after 250 cycles of plating/stripping followed by 10 min of potentiostatic deposition at −1.0 V versus AgQRE (Figure 5e), the Mg KLL spectrum shows a high signal of metallic Mg, corroborating the successful Mg metal deposition. However, the Ti substrate is still detectable as observed in the Ti 2p spectrum, which means that the Mg deposit is not totally covering the substrate surface or it is extremely thin. Scanning electron microscopy images of the Mg deposits (Figure S12 and S13, Supporting Information) confirm the non-fully covering nature of the Mg deposit. The C 1s and F 1s spectra show the same features as for the other electrodes in Figure 5 indicating the formation of the same chemical species and environments. Nonetheless, it contains more carbonate (≈10 at.%) than the electrode shown in Figure 5d, which can be explained by further electrolyte degradation over 250 cycles and potentiostatic deposition. The O 1s spectrum displays the characteristic signature of the Ti substrate, with a decreased intensity. The Mg/O ratio, considering the presence of C-O, COO, CO_3 groups and TFSI, indicates the formation of a mixture of $Mg(OH)_2$ (≈23 at.%) and MgO (≈13 at.%). The formation of MgO is mostly related to the deposition of metallic Mg and is due to the electrolyte degradation on the fresh Mg surface.

Electrodeposition of Mg was further investigated using electrochemical quartz crystal microbalance (EQCM, **Figure 7** and Figure S14). Similar CV curves were obtained as compared to Figure 6a and the CE improves to 88% after the second cycle (CV2) from an initial value of 82% for the first cycle. However, by contrast with the previous data, a gradual decrease of the CE reaching 70% after 20 cycles was recorded, most likely due to the cell configuration and possible contamination of the electrolyte upon time (open cell operated within an Ar filled glove box). It is also worth noting that the overall plating/stripping kinetics is improving upon cycling, with the slopes of the reduction and oxidation waves becoming increasingly steeper. The overpotential between plating and stripping (≈400 mV), however, remains stable and is higher than with Ti electrodes (<200 mV, Figure 6a), suggesting lower nucleation overpotential on Ti than on Pt substrates, confirming the importance of the crystallographic lattice matching considerations.

The evolution of the mass accumulated at the surface of the Pt coated quartz is displayed in Figure 7b for the first five cycles. Even though a maximum coulombic efficiency of 88% was recorded, the mass reversibility evaluated using the Sauerbrey's equation is close to 100% after the third cycle, indicating that the mass being deposited upon reduction (plating) is removed upon oxidation (stripping) after the first cycle. Therefore, continuous growth of passivation layer and/or accumulation of dead Mg during cycling, if any, could not be recorded by EQCM,

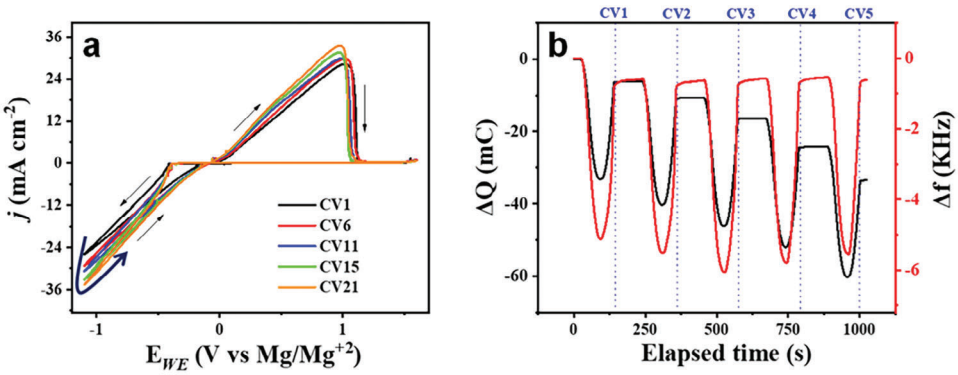

Figure 7. a) Electrochemical behavior of a platinum coated EQCM sensor cycled against a Mg electrode with 25 mV s^{-1} CV scan rate with 0.1 M $Mg(TFSI)_2$ in G1:G2 electrolyte with 130 mM of $Mg(butyl)_2$. b) Evolution of the charge (in mC) and frequency (KHz) during the first five CV cycles.

suggesting that the origin of the coulombic inefficiency is related to irreversible reduction processes associated with the formation of soluble or gaseous products. The absence of dead Mg is also in agreement with the absence of Mg metal from XPS data performed on electrodes after stripping scan. During the first cycle, an irreversible mass accumulation of ≈0.7 µg is evaluated and is tentatively ascribed to both the formation of a passivation layer and to the irreversible formation of Pt_xMg_y alloy identified by X-Ray diffraction (Figure S15, Supporting Information).

2.4. The Influence of the Electrolyte Bulk Physico-Chemical Properties

Among other important parameters influencing the electrochemical performances in batteries, the electrolyte ionic conductivity (in mS cm^{-1}), the nature of the cation solvation shell and the cation transference number are key factors determining the redox process kinetics. While our results demonstrated that lower salt concentration is beneficial for Mg plating / stripping reversibility and kinetics, one can foresee such low salt concentration (0.1 M) to be detrimental in terms of ionic conductivity. Indeed, rather low ionic conductivities were measured (**Figure 8a**) for 0.1 M solution with ≈0.4 mS cm^{-1} for temperatures ranging from 10 to 60 °C. As expected, the ionic conductivity increases with the salt concentration, values at 0.4 M ranging from 3.0 up to 3.8 mS cm^{-1} when the temperature is varied between 10 and 60 °C. Raman spectroscopy measurements were carried out in order to obtain more information regarding the coordination chemistry of the $TFSI^-$ anion (Figure S10, Supporting Information) at these two concentrations. Indeed, the strong Raman band of the $TFSI^-$ anion at ≈740 cm^{-1}, corresponding to the expansion and contraction mode of the whole anion, is commonly used for analysis of ion-ion interactions in electrolytes.[37] From our measurements, the bands are centered at ≈737 cm^{-1} with a certain dissymmetry in their shapes being observed, but no relevant change in the peak position could be detected between 0.1 and 0.4 M $Mg(TFSI)_2$ concentrations (black and pink lines, respectively). DFT calculations of the Raman frequencies for the free $TFSI^-$ anion and the $MgTFSI^+$ CIP were done for both $TFSI^-$ isomers, giving 738.57 and 737.68 cm^{-1}, respectively, for $TFSI^-$ and $MgTFSI^+$ with the *trans* isomer, and 744.32 and 748.29 cm^{-1}, respectively, with the *cis* isomer. It is therefore, difficult to conclude if the degree of contact ion pair formation is affected within the range of salt concentration in the solvent mixture (G1:G2) inves-

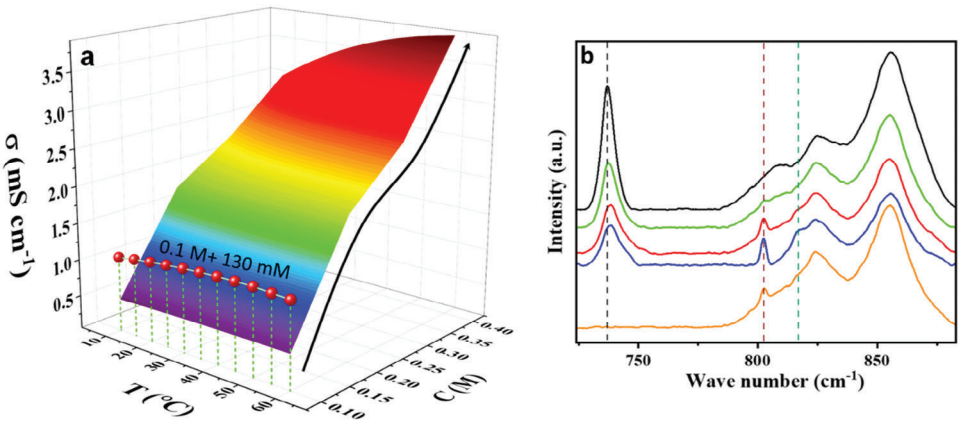

Figure 8. a) Ionic conductivity plots for $Mg(TFSI)_2$ in G1:G2 at different concentrations and temperatures. The influence of the $Mg(butyl)_2$ additive at 0.1 M salt concentration is highlighted with red dots. b) Raman spectra of 0.1 M $Mg(TFSI)_2$ electrolytes with different concentrations of $Mg(butyl)_2$: no additive (black curve), with 50 mM (green curve), with 130 mM (red curve), and with 190 mM (blue curve). The solution without $Mg(TFSI)_2$, containing only 130 mM $Mg(butyl)_2$ in G1:G2 (1:1 vol) is shown for sake of comparison (orange curve).

tigated in this study (Figure S10, Supporting Information), but seems to indicate prevalence of *trans*-TFSI based species.

Nevertheless, upon gradual addition of $Mg(butyl)_2$, a clear splitting of the ≈737 cm^{-1} peak with an additional band appearing at higher wavenumbers, spreading up to 750 cm^{-1}, is observed (Figure 8b), which implies that a $TFSI^-$ fraction is involved in coordinated species and/or its conformational change is triggered. Despite the agreement of the new band with the DFT calculated frequencies when considering the *cis* isomers, it does not necessarily correspond to an increased formation of CIP with the cation. Indeed, increased presence of CIPs is expected to result in higher degree of anion decomposition at the interface with more anion decomposition products in the interphase, which was not observed form XPS data. In addition, the formation of CIPs significantly decreases the mobility of both charge carriers in solution leading to lower ionic conductivity, but here higher ionic conductivities are measured with $Mg(butyl)_2$ (Figure 8a). We thus tentatively ascribe the splitting in the $TFSI^-$ band with additional contribution at higher wavenumbers arising from an interaction with the $Mg(butyl)_2$.

A coordination of the anion is expected to affect the overall mobility of the latter, and thus, the cation transference number (T^+) was evaluated using the Bruce–Vincent method.[39] Potentiostatic polarization measurements were conducted with an applied potential of 100 mV in symmetric Swagelok cell with two Mg disks until the current reached a steady state (I_{ss}). Electrochemical impedance spectroscopy was performed before and after the potentiostatic polarization in order to evaluate the initial and the steady-state interfacial resistance (R_0 and R_{ss}, respectively). The T^+ was calculated according to:

$$T^+ = \frac{I_{ss} \cdot \left(\Delta V - I_0 R_0\right)}{I_0 \cdot \left(\Delta V - I_{ss} R_{ss}\right)} \quad (1)$$

where ΔV is the applied potential and I_0 and I_{ss} are the initial and steady state currents, respectively.

Values for T^+ were calculated to be 0.12, 0.18, and 0.22, respectively for $Mg(TFSI)_2$ electrolytes containing 50, 130, and 190 mM of $Mg(butyl)_2$ indicating that the addition of $Mg(butyl)_2$ results in an increase in the cation transference number, in agreement with the $Mg(butyl)_2$ being involved to some extent in the anion coordination, thus impeding its mobility. It is important to stress out that, since different cationic species can be expected in these electrolytes, the term transference number (T^+) is preferred here instead of t^+ (transport number, used for single cationic species). Furthermore, since the measurements are performed with relatively high salt concentrations, the term "limiting current fraction", F^+ would be more appropriate. While the measured values should be considered as a qualitative estimate of the ratio between the cationic and anionic species mobility in solution, it does provide a relevant trend in the design of new electrolyte formulations. Here, although the values are rather low (as expected for divalent cation based solutions) and the most mobile species remain the anionic ones, the combined increase of the cation transference number and ionic conductivity upon addition of $Mg(butyl)_2$ are playing a major role in the significant improvement of the kinetics and reversibility of Mg metal anode in $Mg(TFSI)_2$ electrolytes. However, the rather limited anodic stability of $Mg(butyl)_2$ (Figure S17, Supporting Information) call for future development of alternative anion coordinating agents.

3. Conclusion

In summary, several parameters affecting the voltage hysteresis between plating and stripping of Mg in $Mg(TFSI)_2$ G1:G2 electrolytes and the overall kinetics were evaluated. First, the crystal structure of the substrate was found to significantly impact the Mg electrodeposition and higher plating kinetics was recorded with Ti electrodes which have similar hexagonal close packed crystal structure and lattice parameters to Mg, also resulting in a lower nucleation overpotential. Pt electrodes, often used for Mg plating studies, having quite different crystal structure and lattice parameters result in slightly higher nucleation overpotential compared to Ti. Furthermore, the formation of a Pt_xMg_y alloy, demonstrated in this work, is expected to favor interfacial processes while impairing the Mg deposit adherence.

The reversibility of Mg plating/stripping was also significantly improved by use of low salt concentrations and addition of $Mg(butyl)_2$. The salt concentration was found to mainly impact the composition of the passivation layer, with interphases richer in solvent-based decomposition products at low salt concentration, as opposed to interphase richer in anion decomposition products and more resistive for higher concentrations. The influence of $Mg(butyl)_2$ on the other hand appeared to be much more complex than being a mere scavenging agent, as commonly assumed. Indeed, addition of $Mg(butyl)_2$ lead to much thinner interphases with limited inorganic / anion decomposition products, yet with some amounts of MgO and $Mg(OH)_2$, further highlighting the fact that the water scavenging effect of $Mg(butyl)_2$ is rather limited. More importantly, $Mg(butyl)_2$ was found to interact with the anion in solution, impeding its mobility and causing an enhanced cation transference number (or more accurately a limiting current fraction of cationic species). Therefore, this work paves the way toward better electrolyte design with improved mobility of electroactive cationic species. Such development is crucial for multivalent cation-based battery chemistries, where anions are always expected to be significantly more mobile than the electroactive cationic species.

4. Experimental Section

Electrolyte Preparation: The electrolyte was composed of magnesium bis(trifluoromethanesulfonyl)imide, $Mg(TFSI)_2$, (99.5% purity, Solvionic) at different concentrations dissolved in a 1:1 vol mixture of Dimethoxyethane; monoglyme (DME, from Sigma-Aldrich, anhydrous, 99.0%) and Diethyleneglycol dimethylether; diglyme (G2, from Sigma-Aldrich, anhydrous, 99.7%). The salt was dried under vacuum for 12 h at 90 °C. The solvents were dried over molecular sieves (3 Å from Alfa Aesar) for a minimum of 2 days. The water content of the electrolyte was below 5 ppm measured by Karl Fischer titrations inside a glove box. A total of 400 µL of electrolyte was used in each cell.

Electrochemical Measurements: The 3-electrode Swagelok cells with T-shape were assembled with a working electrode (WE) composed of a Nickel, stainless-steel (SUS316L) or titanium disks (Goodfellow, Ø10 mm), a magnesium disk (99.98%, Mateck) as a counter electrode (CE) and a silver wire (Sigma Aldrich) as quasi-reference electrode. A cellulose separator was used. All cells were assembled inside an argon-filled glovebox with O_2 and H_2O concentrations below 1 ppm and tested using a

Bio-Logic VSP300 potentiostat. The electrochemical protocol includes two or three consecutive steps depending on the electrolyte being used: 1) the cells were connected at open circuit voltage (OCV) for 2 h. 2) Only for electrolytes without $Mg(butyl)_2$: Galvanostatic Cycling with Potential Limitation (GCPL) was applied as conditioning step for 50 cycles at 0.1 mA cm^{-2} with two constraints, potential limitation −4 to 2 V and 10 minutes for each cycle. 3) The cells were cycled between 0.4 and −3.0 V (vs Ag_{QRE}) or between 1.1 and −0.3 V (vs Mg metal) with a scan rate of 25 mV s^{-1} with −5 or −3 mA as a current limitation at reduction using a Modular Potentio (MP) technique.

X-Ray Photoelectron Spectroscopy Analysis: The cells were disassembled inside an Ar-filled glovebox and the recovered electrodes were washed with dry DME before letting it dry in the glovebox for a few hours. Thermo Scientific ESCALAB 250 spectrometer equipped with an argon-filled glove box, to maintain the samples under inert atmosphere during all times of preparation to their analysis, was utilized. XPS measurements were performed with a focused monochromatized Al Kα radiation ($h\nu$ = 1486.6 6 eV) and the spectra were recorded with pass energy of 20 eV and 600 µm spot size. The analysis was done using the standard charge compensation and the analysis chamber pressure was maintained at ≈2 × 10^{-7} mbar. The binding energy scale was calibrated using the C 1 s peak at 285 eV associated with adventitious hydrocarbon. The data were fitted and analyzed using CasaXPS software with the relative sensitivity factor (RSF) of the ESCALAB database.

Time-of-Flight Secondary Ion Mass Spectrometry (ToF-SIMS): ToF-SIMS analysis was conducted using a TRIFT V Nano ToF II Tandem MS (Physical Electronics, Chanhassen, MN, USA) equipped with a 30 kV Bi_n^{q+} – LMIG (Liquid Metal Ion Gun) primary ion gun. Samples were transferred from the glove box to the spectrometer in a transfer vessel to avoid any exposure to air. The same experimental conditions were maintained for all surface analyses, allowing for semi-quantitative comparisons of peak intensity ratios. The LMIG gun was configured to deliver Bi_3^{++} primary ions with a DC current of 12 nA over a 50 × 50 μm^2 raster size. The mass range was set between 0 and 2000 m/z, with the number of frames set to 30 (dose: 2.2 × 10^{12} ions/cm^2). For all analyses, charge compensation (with low dose of e^- and/or Ar^+) was applied to limit charging effects. Depth profile experiments (series of 40 "analysis/sputtering" cycles) were performed in negative polarity using the same previous analysis conditions (with 20 frames) and a 5 kV Ar^+ gas gun for etching (with a sputtering time of 10 s for each cycle, over a 300 × 300 μm^2 area and a DC current of 150 nA). ToF-SIMS data were processed using ToF-DR software (supplied by Physical Electronics). Negative polarity mass spectra were calibrated using C_2^- (*m/z* 24.00), F^- (*m/z* 19.00), and C_2H^- (*m/z* 25.01) peaks, and positive polarity ones using Na^+ (*m/z* 23.00), Mg^+ (*m/z* 23.98) and MgH^+ (*m/z* 24.99) peaks. For the graphical representation of depth-profiles, the intensity of the secondary ions of interest was normalized related to the total ion counts.

Electrochemical Quartz Crystal Microbalance (EQCM): A three-electrode EQCM cell setup was assembled with a Pt quartz crystal working electrode (WE) (AT-Cut, 8.98 MHz), a magnesium ribbon (99.98%, Mateck) counter electrode (CE), and another thinner magnesium ribbon (99.98%, Mateck) as quasi- reference electrode. The electrolyte, composed of 0.1 M $Mg(TFSI)_2$ in G1:G2 1:1 vol mixture with 130 mM $Mg(butyl)_2$ as an additive, was used to characterize the electrochemical magnesium deposition and dissolution by EQCM. All cell fabrications and electrochemical measurements were conducted in Ar filled glove box with O_2 and H_2O concentrations below 1 ppm and tested using a Bio-Logic SP200 potentiostat, connected with a SEIKO EG&G QCM922A as an external system equipped with resonance frequency change and motional resistance change detectors. The electrochemical protocol includes three consecutive steps: 1) the cells were connected at open circuit voltage (OCV) for 2 h. 2) The cells were then cycled between 1.6 and −1.1 V (vs Mg metal) with a scan rate of 25 mV s^{-1} using a Cyclic voltametric (CV) technique. Subsequently corresponding mass change of the working electrode was monitored by the change in Resonance frequency (Δf, measured in the range of ±20 KHz) and the viscoelastic impact was qualitatively monitored by the change in motional resistance (ΔR, measured in the range of ±2 KΩ) of the QCM system.

Raman Spectroscopies: Raman spectra were recorded using a LabRam HR800 system in backscattering geometry with a spectral resolution of 2 cm^{-1} using a 785 nm laser as the excitation source. Data were typically averaged over ten scans of 30 s each and recorded at room temperature for all the electrolytes. All bands in the resulting spectra were fitted as Voigt functions, typically with a unity Gaussian by width, using Origin Software.

Ionic Conductivity Measurements: Ionic conductivity measurements were performed using a FRA-based Multiplexed Conductivity Meter MCM 10 (BioLogic Science Instruments) from 10 to 60 °C (5 °C steps with 5 min equilibration time).

Density Functional Theory Calculations: Geometries of the $TFSI^-$ anion and the $MgTFSI^+$ contact ion pair were optimized in gas phase at M06-2X/aug-cc-pVDZ level of theory with Grimme's D3 empirical dispersion correction using ORCA 5.0.3 package.[40] Final structures were verified as being energy minima, and further used as inputs for calculation of the Raman frequencies at the same level of theory.

Supporting Information

Supporting Information is available from the Wiley Online Library or from the author.

Acknowledgements

M.R. and T.P. contributed equally to this work. A.P. gratefully acknowledges funding from the European Research Council (ERC) under the European Union's Horizon 2020 Research and Innovation Programme (grant agreement No. 101089281). A.P., T.P., D.S.T. and A.R.G. acknowledge the Spanish Agencia Estatal de Investigación Severo Ochoa Programme for Centres of Excellence in R&D (CEX2023-001263-S). R.D. thanks the French National Research Agency (STORE-EX Labex Project ANR-10-LABX-76-01) for financial support. M.R. acknowledges the European Union H2020-MSCA-COFUND Program for grant agreement #945357 (DESTINY project). Alistore-European Research Institute is gratefully acknowledged for financial support through the postdoc grant to C.B.

Conflict of Interest

The authors declare no conflict of interest.

Data Availability Statement

The data that support the findings of this study are available from the corresponding author upon reasonable request.

Keywords

additive, electrolyte, magnesium battery, metal anode, passivation layer

Received: April 8, 2024
Revised: August 18, 2024
Published online:

[1] World Energy Council, "Five steps to energy storage-innovation insights brief", https://inis.iaea.org/search/search.aspx?orig_q=RN:52024931, (accessed: June 2020).
[2] H. Zhang, L. Qiao, M. Armand, *Angew. Chem.* **2022**, *61*, 202214054.
[3] R. Mohtadi, F. Mizuno, *Beilstein J. Nanotechnol.* **2014**, *5*, 1291.

[4] D. Aurbach, Z. Lu, A. Schechter, Y. Gofer, H. Gizbar, R. Turgeman, Y. Cohen, M. Moshkovich, E. Levi, *Nature.* **2000**, *407*, 724.
[5] K. A. See, K. W. Chapman, L. Zhu, K. M. Wiaderek, O. J. Borkiewicz, C. J. Barile, P. J. Chupas, A. A. Gewirth, *J. Am. Chem. Soc.* **2016**, *138*, 328.
[6] P. Canepa, S. Jayaraman, L. Cheng, N. N. Rajput, W. D. Richards, G. S. Gautam, L. A. Curtiss, K. A. Persson, G. Ceder, *Energy Environ. Sci.* **2015**, *8*, 3718.
[7] C. J. Barile, E. C. Barile, K. R. Zavadil, R. G. Nuzzo, A. A. Gewirth, *J. Phys. Chem. C.* **2014**, *118*, 27623.
[8] S. Y. Ha, Y. W. Lee, S. W. Woo, B. Koo, J. S. Kim, J. Cho, K. T. Lee, N. S. Choi, *ACS Appl. Mater. Interfaces.* **2014**, *6*, 4063.
[9] I. Shterenberg, M. Salama, H. D. Yoo, Y. Gofer, J.-B. Park, Y.-K. Sun, D. Aurbach, *J. Electrochem. Soc.* **2015**, *162*, A7118.
[10] S. Terada, T. Mandai, S. Suzuki, S. Tsuzuki, K. Watanabe, Y. Kamei, K. Ueno, K. Dokko, M. Watanabe, *J. Phys. Chem. C.* **2016**, *120*, 1353.
[11] J. G. Connell, B. Genorio, P. P. Lopes, D. Strmcnik, V. R. Stamenkovic, N. M. Markovic, *Chem. Mater.* **2016**, *28*, 8268.
[12] A. Kopač Lautar, J. Bitenc, T. Rejec, R. Dominko, J. S. Filhol, M. L. Doublet, *J. Am. Chem. Soc.* **2020**, *142*, 5146.
[13] N. N. Rajput, X. Qu, N. Sa, A. K. Burrell, K. A. Persson, *J. Am. Chem. Soc.* **2015**, *137*, 3411.
[14] J. D. Forero-Saboya, E. Marchante, R. B. Araujo, D. Monti, P. Johansson, A. Ponrouch, *J. Phys. Chem. C.* **2019**, *123*, 29524.
[15] S. Fletcher, C. S. Halliday, *J. Electroanal. Chem.* **1983**, *159*, 267.
[16] J. D. Forero-Saboya, D. S. Tchitchekova, P. Johansson, M. R. Palacín, A. Ponrouch, *Adv. Mater. Interfaces.* **2021**, *9*, 2101578.
[17] E. R. Cooper, M. Li, I. Gentle, Q. Xia, R. Knibbe, *Angew. Chem., Int. Ed.* **2023**, *62*, 202309247.
[18] T. Dickinson, A. F. Povey, P. M. A. Sherwood, *J. Electron. Spectros. Relat. Phenomena.* **1973**, *2*, 441.
[19] B. J. Tielsch, J. E. Fulghum, *Surf. Interface Anal.* **1997**, *25*, 904.
[20] A. Cros, *J. Electron. Spectros. Relat. Phenomena.* **1992**, *59*, 1.
[21] T. L. Barr, *J. Vac. Sci. Technol., A.* **1989**, *7*, 1677.
[22] W. M. Lau, *J. Appl. Phys.* **1989**, *65*, 2047.
[23] A. Dane, U. K. Demirok, A. Aydinli, S. Suzer, *J. Phys. Chem. B.* **2006**, *110*, 1137.
[24] G. Ertas, S. Suzer, *Surf. Interface Anal.* **2004**, *36*, 619.
[25] F. Karadas, G. Ertas, S. Suzer, *J. Phys. Chem. B.* **2004**, *108*, 1515.
[26] S. Suzer, *Anal. Chem.* **2003**, *75*, 7026.
[27] G. Ertas, U. Korcan Demirok, S. Suzer, *Appl. Surf. Sci.* **2005**, *249*, 12.
[28] A. Baskin, D. Prendergast, *J. Phys. Chem. C.* **2016**, *120*, 3583.
[29] F. Tuerxun, K. Yamamoto, M. Hattori, T. Mandai, K. Nakanishi, A. Choudhary, Y. Tateyama, K. Sodeyama, A. Nakao, T. Uchiyama, M. Matsui, K. Tsuruta, Y. Tamenori, K. Kanamura, Y. Uchimoto, *ACS Appl. Mater. Interfaces.* **2020**, *12*, 25775.
[30] G. Agarwal, J. D. Howard, V. Prabhakaran, G. E. Johnson, V. Murugesan, K. T. Mueller, L. A. Curtiss, R. S. Assary, *ACS Appl. Mater. Interfaces.* **2021**, *13*, 38816.
[31] Y. Yu, A. Baskin, C. Valero-Vidal, N. T. Hahn, Q. Liu, K. R. Zavadil, B. W. Eichhorn, D. Prendergast, E. J. Crumlin, *Chem. Mater.* **2017**, *29*, 8504.
[32] Y. Zhao, A. Du, S. Dong, F. Jiang, Z. Guo, X. Ge, X. Qu, X. Zhou, G. Cui, *ACS Energy Lett.* **2021**, *6*, 2594.
[33] M. S. Ding, T. Diemant, R. J. Behm, S. Passerini, G. A. Giffin, *J. Electrochem. Soc.* **2018**, *165*, A1983.
[34] H. D. Yoo, S. D. Han, I. L. Bolotin, G. M. Nolis, R. D. Bayliss, A. K. Burrell, J. T. Vaughey, J. Cabana, *Langmuir.* **2017**, *33*, 9398.
[35] J. Zhang, J. Liu, M. Wang, Z. Zhang, Z. Zhou, X. Chen, A. Du, S. Dong, Z. Li, G. Li, G. Cui, *Energy Environ. Sci.* **2023**, *16*, 1111.
[36] M. Yang, N. T. Hahn, J. Connell, I. Bloom, C. Liao, B. J. Ingram, L. Trahey, *Front. Chem.* **2022**, *10*, 966332.
[37] M. Wang, W. Sun, K. Zhang, Z. Zhang, A. Du, S. Dong, J. Zhang, J. Liu, X. Chen, Z. Zhou, F. Li, Z. Li, G. Li, G. Cui, *Energy Environ. Sci.* **2024**, *17*, 630.
[38] I. Rey, P. Johansson, J. Lindgren, J. C. Lassegues, J. Grondin, L. Servant, *J. Phys. Chem. A.* **1998**, *102*, 3249.
[39] P. G. Bruce, M. T. Hardgrave, C. A. Vincent, *Solid State Ionics.* **1992**, *53*, 1087.
[40] F. Neese, *WIREs Comput. Mol. Sci.* **2012**, *2*, 73.